Supplemental Material can be found at:
http://www.jlr.org/content/suppl/2010/07/08/jlr.M008870.DC1.html

Lipid mapping of colonic mucosa by cluster TOF-SIMS imaging and multivariate analysis in *cftr* knockout mice[S]

**Marc Brulet,[1,]* Alexandre Seyer,[1,]* Aleksander Edelman,[†] Alain Brunelle,* Janine Fritsch,[†]
Mario Ollero,[2,]*[,†] and Olivier Laprévote*[,§]**

Centre de Recherche de Gif,* Institut de Chimie des Substances Naturelles, CNRS, 91198 Gif-sur-Yvette, France; Inserm,[†] U845, Faculté de Médecine Paris Descartes, Paris, France; and Chimie Toxicologie Analytique et Cellulaire,[§] EA 4463, Faculté des Sciences Pharmaceutiques et Biologiques, Université Paris Descartes, Paris, France

Abstract The *cftr* knockout mouse model of cystic fibrosis (CF) shows intestinal obstruction; malabsorption and inflammation; and a fatty acid imbalance in intestinal mucosa. We performed a lipid mapping of colon sections from CF and control (WT) mice by cluster time of flight secondary-ion mass spectrometry (TOF-SIMS) imaging to localize lipid alterations. Data were processed either manually or by multivariate statistical methods. TOF-SIMS analysis showed a particular localization for cholesteryl sulfate at the epithelial border, C16:1 fatty acid in Lieberkühn glands, and C18:0 fatty acid in *lamina propria* and submucosa. Significant increases in vitamin E (vE) and C16:0 fatty acid in the epithelial border of CF colon were detected. Principal component analysis (PCA) and partitioning clustering allowed us to characterize different structural regions of colonic mucosa according to variations in C14:0, C16:0, C16:1, C18:0, C18:1, C18:2, C20:3, C20:4, and C22:6 fatty acids; phosphatidylethanolamine, phosphatidylcholine, and phosphatidylinositol glycerolipids; cholesterol; vitamin E; and cholesteryl sulfate. PCA on spectra from Lieberkühn glands led to separation of CF and WT individuals. This study shows for the first time the spatial distribution of lipids in colonic mucosa and suggests TOF-SIMS plus multivariate analyses as a powerful tool to investigate disease-related tissue spatial lipid signatures.—Brulet, M., A. Seyer, A. Edelman, A. Brunelle, J. Fritsch, M. Ollero, and O. Laprévote. **Lipid mapping of colonic mucosa by cluster TOF-SIMS imaging and multivariate analysis in *cftr* knockout mice. *J. Lipid Res.* 2010.** 51: **3034–3045.**

Supplementary key words time of flight secondary-ion mass spectrometry • mass spectrometry • K-mean • partitioning clustering • principal component analysis

The morphology of colonic mucosa can be a crucial parameter in the characterization of diverse diseases, from cancer, to Crohns disease, to inflammatory bowel disease, to diverticular disease, to microscopic colitis, to cystic fibrosis, and a checkpoint in the evaluation of potential therapies. Cystic fibrosis (CF), an autosomal recessive inherited disorder caused by mutations in the cystic fibrosis transmembrane regulator (*CFTR*) gene. Among other symptoms, it is characterized by meconium ileus, one of the earliest manifestations, and in adults, distal intestinal obstruction (1), abnormal absorption and assimilation of nutrients (2), and chronic intestinal inflammation (3, 4). CFTR is mainly expressed in colonic crypts and largely contributes to Cl^- and fluid secretion in this section of the intestine (5). Among the different CF animal models developed, the exon 10-knockout represents a particularly useful model to address the gastrointestinal aspects of the disease. CF mice show mucus accumulation in intestinal crypts and subsequent lethal obstruction (6), as well as increased inflammation markers (7). Yet the pathogenesis of these conditions is not clear. The functions of CFTR, a chloride channel, in the intestine include fluid secretion and pH regulation by modulation of Cl^-, Na^+, and bicarbonate transport through the epithelium (8). However, these two functions are not sufficient to explain all the pathologic manifestations associated with CF.

This work is supported by Agence Nationale de la Recherche Grant EICO-CF; European Commission Grants NEUPROCF (FP6) and COMPUTIS (LSHG-CT2005-518194); associations Vaincre la Mucoviscidose and Mucoviscidose ABCF; Legs Poix-University of Paris 5; and PhD research fellowship (A.S) from Institut de Chimie des Substances Naturelles (CNRS).

Manuscript received 31 May 2010 and in revised form 8 July 2010.

Published, JLR Papers in Press, July 8, 2010
DOI 10.1194/jlr.M008870

Abbreviations: CF, cystic fibrosis; CFTR, cystic fibrosis transmembrane regulator; CS, cholesteryl sulfate; GA, genetic algorithm; KO, knockout; LG, Lieberkühn glands; MSI, mass spectrometry imaging; PC, phosphatidylcholine; PC1–4, principal component 1–4; PCA, principal component analysis; PE, phosphatidylethanolamine; PI, phosphatidylinositol; ROI, region of interest; ST, sulfatide; TOF-SIMS, time of flight secondary-ion mass spectrometry; vE, vitamin E; WT, wild-type.

[1] M. Brulet and A. Seyer contributed equally to this work.

[2] To whom correspondence should be addressed.
e-mail: mario.ollero@icsn.cnrs-gif.fr

[S] The online version of this article (available at http://www.jlr.org) contains supplementary data in the form of eight figures.

Another aspect that is hardly explained as a consequence of CFTR dysfunction is the presence of alterations in the metabolism and in the blood and tissue content of certain lipids (9) (polyunsaturated fatty acids (10, 11), phospholipids (12, 13), sphingolipids (14, 15), and cholesterol (16)). Nevertheless, these findings have been addressed by biochemical methods on total tissue homogenates or by chemical imaging of lipid analogs in cell models. As a consequence, little is known about the local distribution in tissue of lipid alterations in CF.

The advent of mass spectrometry-based imaging techniques, namely, MALDI and TOF-SIMS, has opened new perspectives in the combination of morphological analysis and molecule localization. Their particular suitability for the analysis of small molecules opens up the possibility of targeting lipids in the search for mechanistic insights leading to the discovery of therapeutic approaches or biomarkers by these techniques. TOF-SIMS was first developed in the 1960s for surface analysis (17, 18). This technology consists of the bombardment of the sample by a beam of mono- or polyatomic ions, which induces desorption/ionization of secondary ions from the sample surface. Polyatomic ion beams have been used successfully in the analysis of organic surfaces with a resolution of some hundreds of nanometers (19–24), which makes the technology particularly fit for the analysis of tissue sections (19, 22, 25–32). Conversely, MALDI uses a matrix to allow soft desorption/ionization of intact compounds upon laser absorption; it is also adapted to imaging analysis but at a spatial resolution limited to ~50 μm with the current state-of-the-art.

The approach of mass spectrometry imaging (MSI) is usually based on univariate analysis of ion images. This represents a limitation in global studies where there are no particular targeted molecules. Multivariate approaches, like principal component analysis (PCA), allow distinguishing spatial structures and establishing correlations between tissue molecules (33–35). In this study, we performed a thorough analysis of mouse colonic mucosa by TOF-SIMS imaging in tissue samples from CF and wild-type (WT) mice, and we processed the data by PCA and other multivariate approaches. We established the spatial distribution and the covariation of lipids of interest in the tissue. We also evaluated potential differences in lipid content and distribution, which can be attributed to the presence or absence of functional CFTR, between both groups of animals. The results obtained represent the first lipid mapping of colon mucosa, as well as the first lipid imaging study in the context of CF, and establish a starting point for future analyses on those pathologies that target colon.

MATERIALS AND METHODS

Biological material and sample processing

Wild-type (WT) and Cftr-exon 10-knockout (CF) C57BL/6J mice were obtained from the Centre de Distribution, de Typage et d'Archivage Animal (Orléans, France). After weaning, mice were fed a standard laboratory diet and water. Experiments were performed on 8–12-week-old mice in conformity with the Public Health Service (PHS) Policy on Humane Care and Use of Laboratory Animals and in accordance with Necker Faculty of Medicine Animal Care and Use Committee (Paris Descartes University). Animals were sacrificed by cervical dislocation. Colon was harvested, washed in phosphate buffer saline, and snap-frozen in liquid nitrogen. Serial transversal sections (10 μm thick) were cut at −20°C with a CM3050-S cryostat (Leica Microsystems, Nanterre, France) and immediately deposited on 2 in diameter polished silicon wafers (ACM, Villiers-Saint-Frédéric, France) for TOF-SIMS experiments. Samples were dried under vacuum at a pressure of a few hectopascals for 10 min before analysis. Optical images were recorded with an Olympus BX51 microscope (Rungis, France) equipped with 1.25× to 50× lenses and a Color View I camera, monitored by Cell^B software (Soft Imaging System, Münster, Germany). Adjacent tissue sections were stained by hematoxilin-eosin and used as morphology controls. A total of 13 sections of mouse colon were used for the different analyses, 6 corresponding to three WT mice and 7 to three CF mice.

TOF-SIMS imaging

A standard commercial TOF-SIMS IV (ION-TOF, Münster, Germany) reflectron-type TOF mass spectrometer was used for MSI experiments. The primary ion source was a bismuth liquid metal ion gun. Bi_3^+ cluster ions were selected. The ion column focusing mode ensured both a 1–2 μm beam focus and short pulse duration of less than 1 ns. Such short pulses are a prerequisite for high-mass resolution, accurate mass measurements, and structure assignments. Because of the very low initial kinetic energy distribution of the secondary ions, the relationship between the time-of-flight and the square root of the mass-to-charge ratio (m/z) of secondary ions is always linear over the whole mass range. The mass calibration was always internal; signals used for initial calibration were those of C^-, CH^-, C_2^-, and C_2H^- for the negative ion mode. Signals of fatty acid carboxylate ions and deprotonated vitamin E were used for the calibration refinement. Structure attributions or assignments of ion peaks were made according to the instrument resolution ($M/\Delta M = 10^4$, full-width half-maximum [FWHM] at m/z 500), accuracy, and the valence rule. Moreover, mass spectra of reference compounds were recorded and compared with spectra recorded in situ to confirm the assignments. Finally, the biological relevance of the attribution was also taken into account, and many mass assignments were also confirmed or at least reinforced with the help of the literature (20–22, 31, 32, 36–39).

Images were recorded with a field of view of $500 \times 500\ \mu m^2$ and 256×256 pixels, giving a pixel size of $2 \times 2\ \mu m^2$. A color scale bar indicates the amplitude and ion counts of each ion image. The data acquisition and processing software was IonSpec and IonImage (ION-TOF).

Negative ion mode images were successively recorded for each selected area. All the images were recorded with a primary ion fluence (also called primary ion dose density) of 2×10^{12} $ions{\cdot}cm^{-2}$, an ion rate higher than in our usual imaging experiments but still below the so-called static-SIMS limit, which ensured little sample damage and the maximum of intact secondary ion emission (40). A low-energy electron flood gun was activated to neutralize the surface during the analysis (41).

Multivariate analysis

The classical approach in mass spectrometry-based imaging consists of univariate analyses. This approach presents its limitations in studies where there is not an a priori molecular target or in the absence of a known disease marker. The alternative strategy is the use of multivariate analyses, where the effects of more than one statistical variable on the parameter of interest are analyzed simultaneously. Our study was based on two main multivariate techniques: PCA and partitioning clustering.

PCA explores the links between variables and similarities between individuals. It is defined as an orthogonal linear transformation of data to a new coordinate system. The new axes are defined by the eigenvectors of the variance-covariance matrix. Each axis is associated with a linear form that explains the variability of the new axis and a variable that contains coordinates corresponding to the projections of individuals on the axis called 'principal component'. PCA is a powerful technique used to reduce the dimensions of large sets of data. In the present study, the main source of variability within an image is due to chemical compositions of the different parts of the tissue, while between images it corresponds to the WT or CF mouse genotype.

Clustering analyses assign each individual to a subclass (cluster), such that all individuals in a subclass present a degree of similarity. These are unsupervised learning processes based on the calculation of inertia between individuals of the dataset. Inertia is a generalized measure of the variance in the system. The total inertia is equal to the sum of the intraclass inertia and interclass inertia. Intraclass inertia is the amount of inertia of the separate clusters, and interclass inertia is the amount of inertia between clusters. The latter can be seen as a measure of the difference between classes. Therefore, the goal of clustering is to maximize interclass inertia to obtain the most distinct classes possible. The two types of clustering used in this study are partitioning clustering, to regroup pixels in clusters defining biochemical zones, and hierarchical clustering, to classify mice by their spectral similarities.

In addition, we used genetic algorithms, which can serve as an early step in data analysis. This is a supervised learning method that selects a small number of highly predictive variables; in our study, to discriminate WT and CF mice.

Multivariate analyses were carried out on TOF-SIMS-MSI data using Solo+MIA, the standalone versions of PLS_Toolbox and MIA_Toolbox (www.eigenvector.com, Eigenvector Research, Wenatchee, WA) for Matlab (MathWorks, Natick, MA).

Two kinds of datasets were analyzed: the first one corresponding to TOF-SIMS images to characterize different structural regions, and the second one corresponding to concatenated areas of TOF-SIMS spectra to differentiate CF and WT individuals. Both datasets needed a different preprocessing step.

TOF-SIMS image datasets came from colon sections of CF mice. Data acquisition was performed using the IonImage software to generate images from peaks of interest. Import of images to Solo+MIA software was made in binary format. Regions of interest (ROI) were defined manually with the lasso tool. The areas corresponding to the lumen of colon were excluded (56,546 out of 65,536 pixels were included in the example shown in **Figs. 2–5**, which represents about 86.3% of total area). The preprocessing step consisted of centering, scaling, and normalizing using the Euclidian distance. This last step allowed, in this case, a better discrimination of the distinctive histochemical features. A total of 15 variables in the *m/z* range 100–900 were selected for PCA and partitioning clustering (**Table 1**; supplementary Fig. I). They were chosen according to ions of interest cited in the literature (10, 12, 13) and because they possessed a distinct spatial distribution and a reasonable intensity.

The TOF-SIMS-spectra dataset came from 13 colon sections of three WT and three CF mice. Data acquisition for each ROI spectra was performed using the IonSpec software (supplementary Fig. I). All 13 ROI spectra were generated according to the distribution of the *m/z* 253.24 ion (carboxylate ion of palmitoleic acid C16:1n-7), which delineates the glands of Lieberkühn (**Fig. 1**). All spectra were further normalized according to the number of pixels of each ROI spectra. Areas were computed for 12 ions of interest, corresponding to the same as in the image dataset (Table 1), excluding carboxylate ions C14:0 (*m/z* 227.22), C20:3 (*m/z* 305.26), and C22:6 (*m/z* 327.15). The dataset was centered and rescaled prior to PCA.

Principal component analysis

PCA was applied to TOF-SIMS image datasets from colon sections after preprocessing. Score plots show the values for each pixel on the associated principal component axis. The false color scale indicates the level of contribution of each pixel to the axis. Pixels that correspond to the same histochemical structure (i.e., pixels showing similar mass spectra) are expected to have a similar contribution to different principal components, and they appear with the same color. Loading plots show the positive and negative correlations of each original variable with the respective principal component. In the end, it is the coevolution of the original variables that explains the discrimination of pixels on the principal component.

PCA was also applied to TOF-SIMS spectra datasets after preprocessing. Biplots synthesize the information by superimposing the samples (i.e., the spectra) and the original variables (i.e., the selected ion peaks) on a common space. Here we used the PC1-PC2 factorial plane (**Figs. 6** and **7A**). This graph allows visualizing the affinities between the different spectra (representing each individual mouse) and explaining the correlation between the original variables and the principal component.

Partitioning clustering

Partitioning clustering, which was performed by the K-means algorithm on the TOF-SIMS image dataset after preprocessing, assigns each point to the nearest cluster represented by its barycenter. The K-means algorithm requires as input the determination of a number of wished "k" clusters. The algorithm classifies each pixel into one of these "k" clusters either by minimizing the sum of distances from their respective centers or by maximizing interclass distance, which ultimately leads to the most distinct clusters possible.

Hierarchical clustering

After preprocessing, the TOF-SIMS spectra dataset was subjected to hierarchical clustering analysis using the Euclidean metric as the distance metric and Ward's criterion as the agglomerative criterion. In hierarchical clustering, a hierarchy of clusters is represented by a structure (dendrogram) that resembles the shape of a tree. The trunk of the tree corresponds to the cluster regrouping the totality of individuals (i.e., mice) and the leaves to the unique individuals. This graph (Fig. 7B) enables visualizing the similarity between two individuals and/or clusters as a function of the number of branches separating them from a common junction. By cutting off the dendrogram at a specific level, the dataset can be characterized by the corresponding number of classes.

Genetic algorithm analysis

Genetic algorithm (GA) analysis is a supervised learning method that allows the selection of a small number of highly predictive variables among an initial list of variables. In the present study, the initial list of variables was chosen according to known *m/z* values of ions and fragments. GA analysis was performed on TOF-SIMS spectra of ROI corresponding to Lieberkühn glands. Spectra preprocessing is detailed above. From the different random combinations of variables tested by the algorithm, the one that provided the best discrimination between the two classes of mice was chosen. The selected ions were reexamined and validated according to their intensity and spatial distribution characteristics. The final list of ions (**Table 2**) was subsequently subjected to PCA and hierarchical clustering analysis.

TABLE 1. Selected ions for the principal component analysis on TOF-SIMS/MSI data

m/z	Ion Species	Lipid Family	Localization
140.03	$[C_2H_7NO_4P]^-$	PE	LG, border
168.07	$[C_4H_{11}NO_4P]^-$	SM, PC	*Lamina propria*, submucosa
227.22	C14:0[a]	FA	LG
253.24	C16:1	FA	LG
255.25	C16:0	FA	Mucosa
259.07	$[\text{phosphoinositol}]^-$ or ST fragment	ST, PI	Mucosa
279.25	C18:2	FA	Border
281.27	C18:1	FA	Border, LG
283.28	C18:0	FA	*Lamina propria*, submucosa, border
303.26	C20:4[a]	FA	Border, submucosa
305.26	C20:3[a]	FA	LG
327.15	C22:6	FA	Homogeneous distribution
385.39	$[\text{Cholesterol-H}]^-$	ST	LG, border
429.4	$[\text{Vitamin E-H}]^-$	vE	Border
465.35	$[\text{cholesteryl sulfate-H}]^-$	ST	Border

LG, Lieberkühn glands; MSI, mass spectrometry imaging; PC, phosphatidylcholine; PE, phosphatidylethanolamine; PI, phosphatidylinositol; TOF-SIMS, time of flight secondary-ion mass spectrometry; SM, sphingomyelin; ST, sulfatide; vE, vitamin E.

[a] Ion species excluded from the PCA on TOF-SIMS spectra data analysis.

RESULTS

Lipid mapping of mouse colon by univariate analysis

Colon sections from three WT and three CF mice were analyzed by TOF-SIMS in the negative ion mode. Fig. 1 shows images corresponding to the spatial localization of fatty acid carboxylate ions C16:1 (m/z 253.20, Fig. 1A, I), C18:0 (m/z 283.27, Fig. 1C, K), and C18:2 (m/z 279.24, Fig. 1B, J), vitamin E (vE, m/z 429.37, Fig. 1D, L), cholesteryl sulfate (CS, m/z 465.32, Fig. 1E, M), and the sulfatide and/or phosphoinositol fragment (m/z 259.05, Fig. 1F, N) from WT and CF mice (supplementary Fig. II). Note that the detected fatty acid carboxylate ions correspond to both free fatty acids and acyl fragments from more complex molecules. Some ion signatures are characteristic of the *lamina propria* and submucosa (C18:0) of Lieberkühn glands (LG) (C16:0) and the epithelial border (CS, C18:2). This distribution in three regions is illustrated by the merged three-color image (Fig. 1H, P). The distribution of ions corresponding to cholesterol (not shown) and vE is mostly uniform. Arachidonic acid (AA, C20:4, m/z 303.26) was localized to submucosa, *lamina propria*, and border, while its fatty acid precursor (C20:3, m/z 305.26) was mainly present in LG in both WT and CF sections (supplementary Figs. III, IV, V). Although some minor differences in spatial localization were observed between WT and CF colon, they were not consistently present in all individuals. In addition, no significant differences were observed between total spectra from WT and CF mice.

Lipid mapping by PCA on a TOF-SIMS image

The main objective of PCA applied to mass spectrometry imaging data is to identify underlying structures in the (X,Y) space by their spectral similarity, to identify correlations between ions characterizing the main structures, and ultimately, to discriminate different structural areas biologically relevant in the tissue based on their mass spectral fingerprint. For this study, we selected the first four principal components. PC1 accounts for 20.90%, while PC2, PC3, and PC4 capture 14.16, 9.89, and 7.45%, respectively, of total inertia (which represents the relative amount of information captured by each principal component). Their respective spatial distributions are shown in Fig. 2, where each panel shows both the score (left) and loading (right) plot for each principal component. From the score plot it can be inferred that PC1 delineates a structure consistent with the morphology and spanning of Lieberkühn glands (red to yellow pixels), discriminating in a general way the mucosa from the epithelial edge (blue pixels) (Fig. 2A). Dark-blue pixels correspond to those removed from the analysis. The loading plot indicates the contribution of each ion to PC1 (Fig. 2E). In fact, the coevolution of the increased concentration of C14:0, C16:1, and C16:0 with respect to the decreased concentration of CS and C18:0 is responsible for this discrimination. As shown in the corresponding score plot (Fig. 2B), PC2 delineates a structure consistent with the apical part of Lieberkühn glands, as well as some border elements (red to yellow), in contrast with *lamina propria* and submucosa (blue). This is due to increased amounts of phosphoethanolamine (a fragment of PE), an ion detected at m/z 259 and attributed as a fragment of either PI or a sulfated lipid (sulfatide, ST), C18:1 in combination with decreased levels of phosphocholine (fragment of PC and/or SM), as shown in the loading plot (Fig. 2F). PC3 is consistent with the localization of *lamina propria*, border, and submucosa (red-to-yellow pixels on Fig. 2C), mainly due to increased C20:4, C18:0, phosphocholine (fragment of PC and/or SM), vE, C18:1, C18:2, and C16:0, and decreased ST or PI fragment, as shown by the loading plot (Fig. 2G). PC4 is mostly localized at the epithelial edge, the *lamina propria*, and submucosal structures (red-to-yellow pixels), with a contribution of increased cholesterol, C22:6, and phosphoethanolamine (fragment of PE) concomitant with a decrease in CS and C18:2 (Fig. 2D, H). However, the interpretation of the score plot

Supplemental Material can be found at:
http://www.jlr.org/content/suppl/2010/07/08/jlr.M008870.DC1
.html

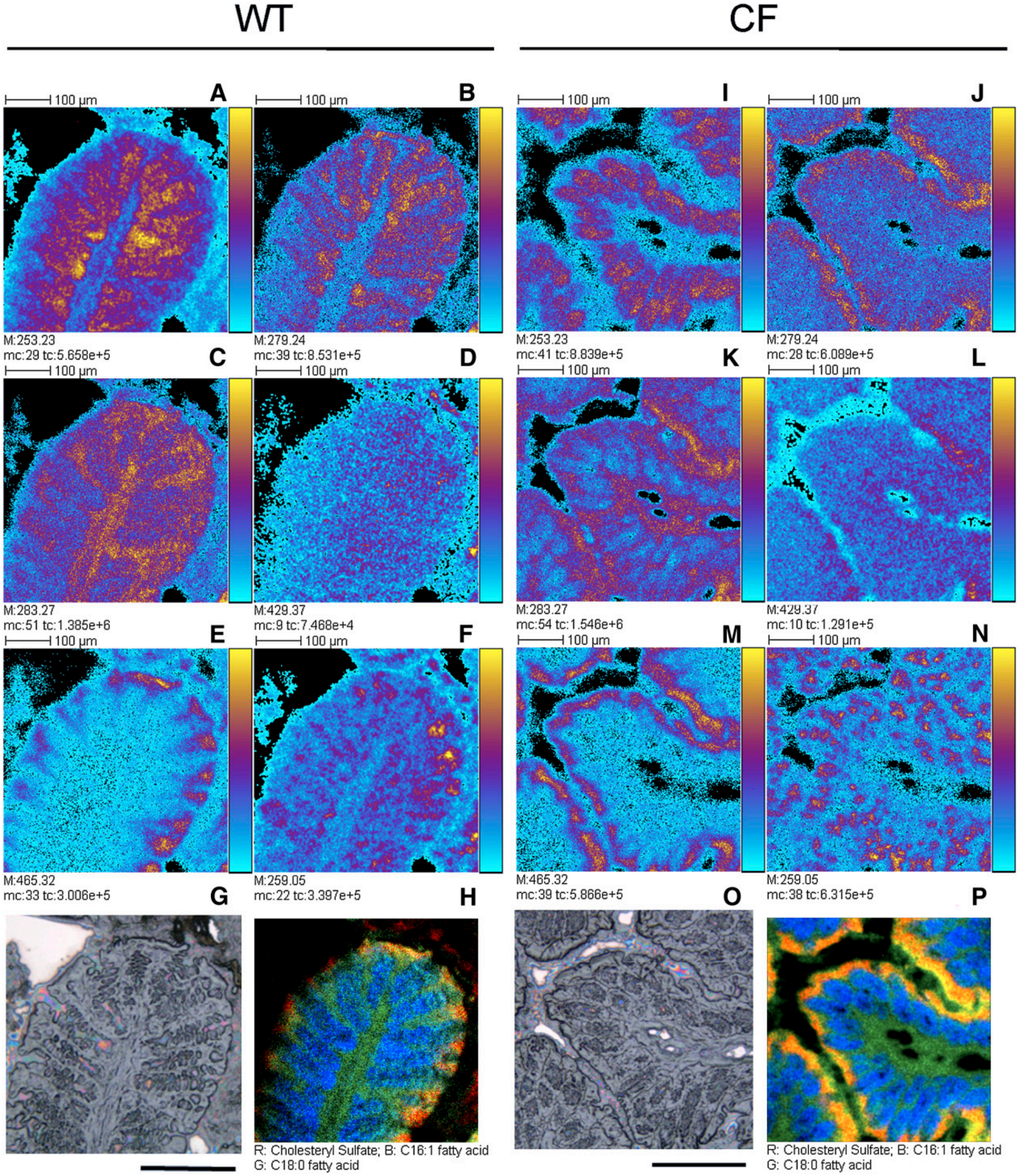

Fig. 1. Localization of individual lipids in WT and CF mouse colonic mucosa. Images from one WT (A–H) and one CF (I–P) mouse colon section are shown. Cluster TOF-SIMS images correspond to C16:1 ($[M\text{-}H]^-$, A and I), C18:0 ($[M\text{-}H]^-$, B and J), C18:2 ($[M\text{-}H]^-$, C and K), vE ($[M\text{-}H]^-$, D and L), CS ($[M\text{-}H]^-$, E and M), sulfated lipid fragment and/or phosphoinositol ($[M\text{-}H]^-$, F and N) are shown. The name of the compound, the *m/z* value of the peak centroid, the maximal number of counts in a pixel (mc), and the total number of counts (tc) are written below each image. The amplitude of the color scales correspond to the interval [0, mc]. G and O: Optical images (bar size = 200 µm). H and P: Three-color overlay for C16:1, C18:0, and CS. CF, cystic fibrosis; CS, cholesteryl sulfate; TOF-SIMS, time of flight secondary-ion mass spectrometry; vE, vitamin E; WT, wild-type.

becomes more and more subjective for the later principal components.

Another way of visualizing the results is to represent the pixels in the space of scores, evaluate the differences between groups of pixels, and define specific biological structures as a function of their spectral similarity. Figure 3 synthesizes the information contained in the principal plane PC1-PC2, represented in the center, where pixels are defined by their coordinates on the PC1 and PC2 axes. The color scale indicates the density of pixels having similarities in their spectra. This plane contains 35.06% of total inertia and embodies three major regions of pixels grouped in

TABLE 2. Ions selected by GA analysis for further PCA and hierarchical clustering analysis

m/z	Ion Species	Lipid Family
109.99	$[CH_3O_4P]^-$	PE, PC, SM
164.92	Fragment	PI
168.08	$[C_4H_{11}NO_4P]^-$	PC, SM
215.92	Fragment	CS, ST
220.91	Fragment	PI, ST
227.22	C14:0 carboxylate	FA
255.25	C16:0 carboxylate	FA
429.40	$[\text{Vitamin E-H}]^-$	VE
861.70	$[\text{TG52:0-H}]^-$	TG

CS, cholesteryl sulfate; GA, genetic algorithm; PC, phosphatidylcholine; PCA, principal component analysis; PE, phosphatidylethanolamine; PI, phosphatidylinositol; SM, sphingomyelin; ST, sulfatide; vE, vitamin E.

clusters (Areas 1, 2, and 3), mainly discriminated by PC1. As seen in Fig. 3, the left cluster (Area 1) is constituted of pixels of the epithelium border region. This cluster covers 5,142 pixels, which represent approximately 9.1% of the total tissue area. The epithelium border is characterized by an increased amount of CS, C18:0, and C18:2, and decreased amounts of C14:0, C16:0, and C16:1 fatty acids compared with the rest of the tissue. The right cluster (Area 2) contains mainly pixels of Lieberkühn glands. This cluster covers 12,788 pixels, which represent approximately 22.6% of the total tissue area. LG are characterized by increased C14:0, C16:0, and C16:1 amounts, and decreased CS and C18:0 amounts compared with the rest of the tissue. This nearly reverse lipid fingerprint, with respect to Area 1, is due to the fact that the PC1 is the main discriminating axis that separates LG from the epithelium border pixel cluster, as can be seen on the PC1-PC2 score plane (Fig. 3, center image). The bottom cluster (Area 3) is mainly generated by pixels from the submucosa and some from the *lamina propria*. This cluster covers 5,695 pixels, accounting for approximately 10.1% of total tissue area. This cluster is mainly carried out by the PC2 on the negative value area. The submucosa is characterized by increased phosphocholine and decreased phosphoethanolamine, ST, or PI fragment, and C18:1 content compared with the rest of the tissue. The last area (Area 4) is characterized by a rather vague contour compared with the three other areas. It is located between Areas 2 and 3 and corresponds to the *lamina propria*. This cluster covers 1,895 pixels, which represent approximately 3.4% of total area, and is characterized by increased phosphocholine and C16:0 content, as well as decreased CS, C18:2, and C18:1 fatty acids, phosphoethanolamine, and ST or PI fragment amounts.

A three-color overlay of the first three principal components provides a better contrast between the different histochemical areas according to their spectral profiles (Fig. 4). The color of pixels is determined by their contribution score on each principal component (red for PC1, green for PC2, and blue for PC3). All different histochemical substructures can be distinguished: *lamina propria* and submucosa are colored in blue-magenta, indicating that these two regions are primarily defined by a positive contribution of PC3 and some PC1; the border is divided into two regions: a light-blue layer in contact with the epithelium, characterized by a positive contribution PC2 and PC3, and a green area in contact with the lumen, probably due to secreted mucus and characterized by a positive contribution of PC2; Lieberkühn glands are mainly yellow colored, indicating major contributions of PC1 and PC2. Some color variation can be observed from yellow-green and yellow-red, characterizing the proximal and distal part of LG, respectively. Finally, some dark-green pixels located inside the glands suggest a contribution of PC2 and PC3, which could be interpreted as the presence of secreted mucus.

Lipid mapping by partitioning clustering on a TOF-SIMS image

In the partitioning clustering study, the K-mean algorithm was used on the same variables as those for PCA (Table 1). The result is shown in Fig. 5 as a palette of images representing the partitioning into 2, 3, 4, and 5 clusters, respectively. The dark-blue area corresponds to pixels of the colon lumen, which were excluded from the analysis. The two-class clustering (Fig. 5A) distinguishes the Lieberkühn glands (brown) from the rest of structures (green). The three-class (Fig. 5B) separates border (light blue) and LG (brown) from *lamina propria* and submucosa (yellow-red). The four-class (Fig. 5C) discriminates the apical part of LG (brown) from the rest of the gland (orange), the *lamina propria* submucosa (green), and the epithelial border (light-blue). The five-class clustering (Fig. 5D) results in the discrimination of a brown area corresponding to the external part contiguous to the lumen, a middle-blue area corresponding to the epithelial border, a green-blue surface corresponding to the *lamina propria* and submucosa, and finally, the LG in two clusters, orange and yellow for the distal and proximal part, respectively. This analysis confirms the results obtained by PCA.

Differences between CF and WT mice are revealed by TOF-SIMS

A semiquantitative analysis of potential differences in lipid content between CF and WT was performed by selecting several ROI from each tissue section and comparing their associated spectra. These regions correspond to the epithelial border, the crypts, and the *lamina propria*, according to the localization of CS, C16:1, and C18:0, respectively. The corrected area for each peak of interest was divided by the number of pixels accounting for each ROI. The C16:0 amount was significantly increased (by 23%) in the border of CF versus WT mice, whereas the vE amount was significantly increased in CF both in the border (by 52%) and in the *lamina propria* (by 52%). The rest of peaks presented no significant differences between the two mouse types.

Discrimination of CF and WT mice by PCA on TOF-SIMS spectra from LG region

To establish a comparison between WT and CF tissues, spectra from selected ROI corresponding to LG from the 13 sections were analyzed by PCA. The choice of this ROI is due to the fact that CFTR is mostly expressed in this area. The ions listed in Table 1 were subjected to PCA

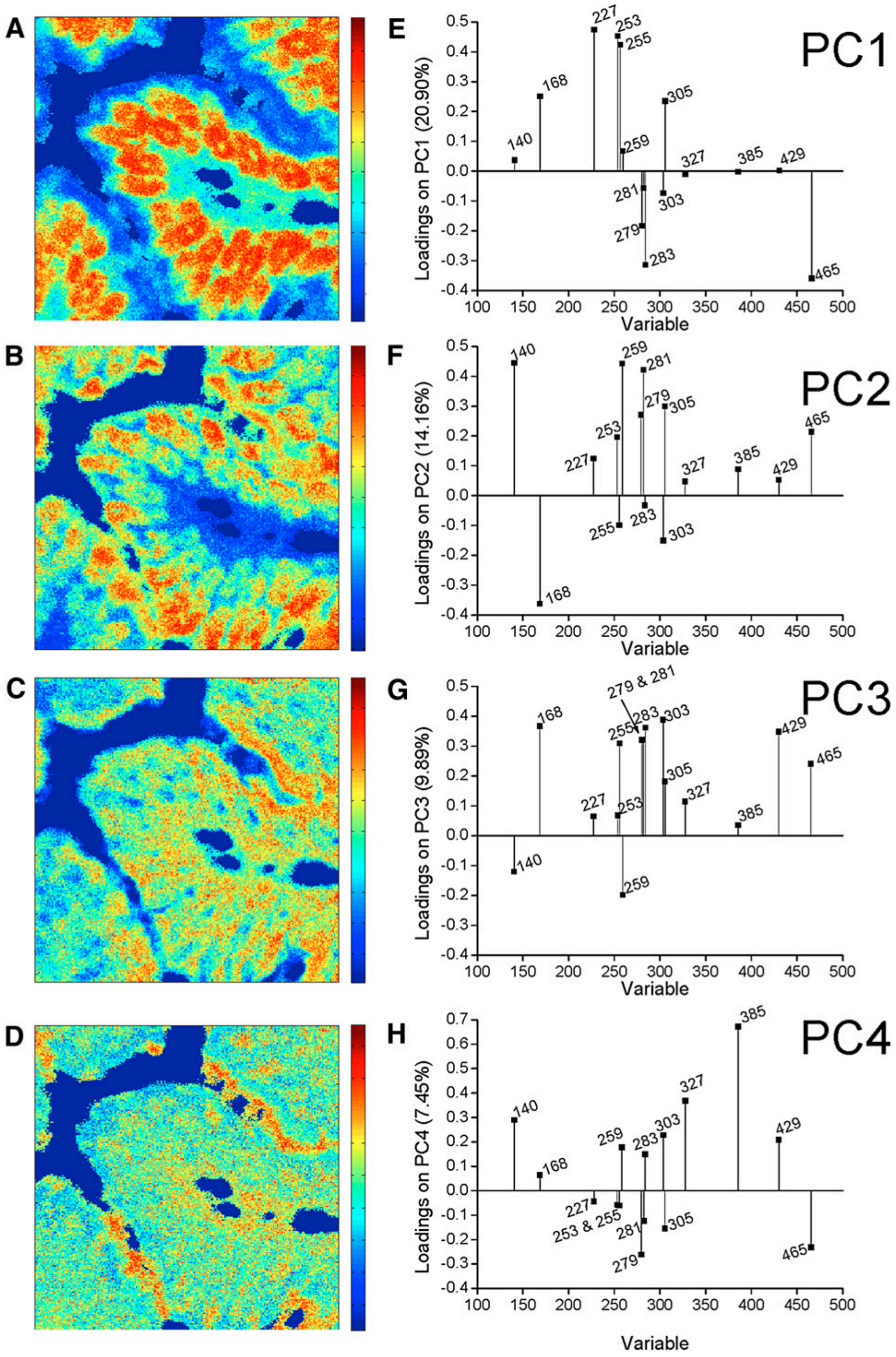

Fig. 2. Score and loading plots of the first four principal components in a CF mouse colon section. Score (left panels) and loading (right panels) plots corresponding to PC1 (A and E), PC2 (B and F), PC3 (C and G), and PC4 (D and H) are represented. CF, cystic fibrosis; PC1–4, principal component 1–4.

analysis. PC1 and PC2, which carry the greatest variance among the 13 sections, account for 41.49% and 20.91% of total inertia, respectively. The three main principal components accumulate 81.65% of total inertia. Assuming that the greatest source of variability between mice corresponds to CFTR expression, this feature is expected to be the main contributor to the potential discrimination between the two classes of mice and should be expressed in the first two principal components. The biplot shown in Fig. 6 synthesizes the results by superimposing the individuals and the original variables (selected ions) on a common space representing the principal plane built from PC1 and PC2, where WT individuals are represented in green and CF in red. Both classes of mice seem to be separated by the first principal component, even though the separation is not very distinct. The main contribution to the separation is due to an increase in CF mice of CS, C16:1, C16:0, phosphoethanolamine, phosphoinositol (PI fragment) or ST,

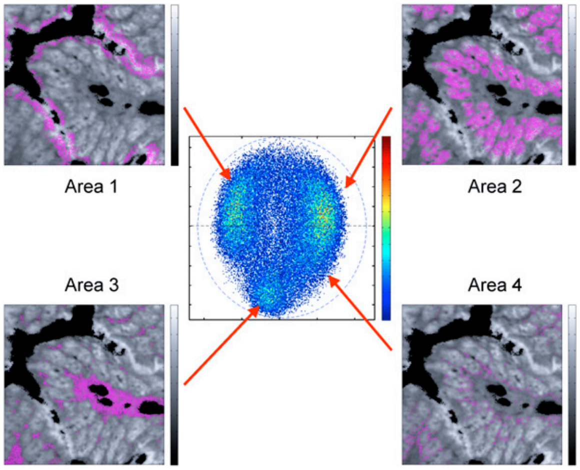

Fig. 3. Distribution of clusters on the PC1 and PC2 plane. Visualization of the four different clusters of pixels manually selected on the principal plane constituted by the two first principal components. Those clusters represent the four main histochemical structures, namely, the epithelial border (Area 1), the Lieberkühn glands (Area 2), the submucosa and *lamina propria* (Area 3), and the *lamina propria* (Area 4). The total ion current image was used to represent the different selected clusters of pixels. The color scale of the center image corresponding to the PC1-PC2 score plot represents the density of pixels having the same PC1 and PC2 score coordinate. PC1–4, principal component 1–4.

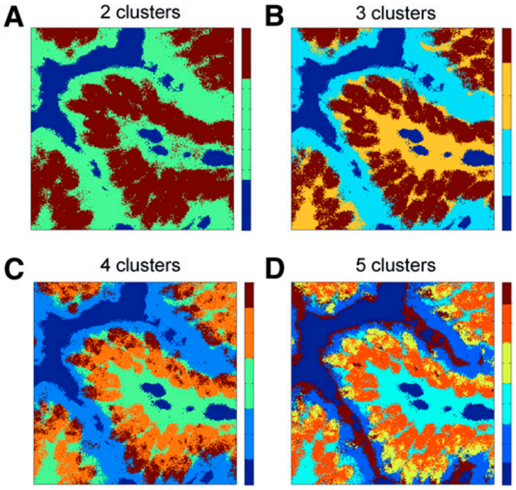

Fig. 5. Distribution of partitioning clusters. Partitioning clustering was performed on a CF mouse colon section using the K-mean algorithm. Images correspond to partitioning into two (A), three (B), four (C), and five (D) clusters. The dark blue area corresponds to pixels excluded from the analysis. CF, cystic fibrosis; PC1–4, principal component 1–4.

phosphocholine, and to a lesser extent, cholesterol and vE, accompanied by a decrease in C18:2.

In addition, PCA and hierarchical clustering were carried out on the 12 ions listed in Table 2. This list was produced by GA analysis, providing the best combinations of variables discriminating WT and CF mice. The PC1-PC2 biplot (Fig. 7A) shows a perfect separation between CF and WT based on the first principal component. These results indicate that CF mice are characterized by increased amounts of C14:0 and C16:0 carboxylate ions (*m/z* 227.22 and 255.25, respectively), vE ion fragment (*m/z* 429.40), and ion fragments (*m/z* 109.99 and 168.07) of different phospholipids (PE, PC, and SM) in LG with respect to WT mice. Hierarchical clustering analysis (Fig. 7B) provided a very satisfactory separation between WT and CF mice present at the first branching. Similarly, different sections from the same mice are paired, indicating that the analysis is reproducible within the same individual.

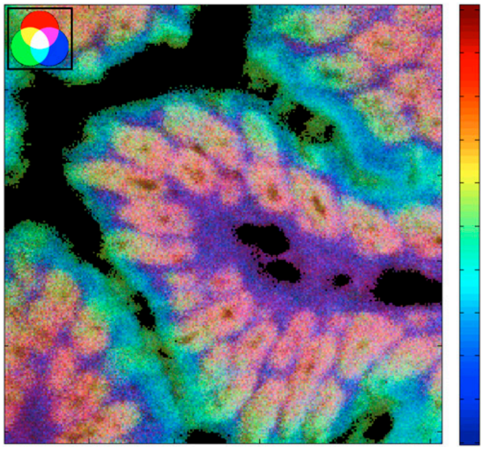

Fig. 4. Overlay of the score images of PC1, PC2, and PC3. The color scale represents the contribution for each pixel on the selected principal axes. Red, green, and blue indicate a strong positive contribution of PC1, PC2, and PC3, respectively. PC1–4, principal component 1–4.

DISCUSSION

In the present work, we combined a mass spectrometry-based lipid imaging method with several multivariate statistical analyses to provide a detailed mapping of lipids in the mouse colon and to establish potential differences in lipid content and distribution between WT and CF mice. As a result, we found a distinct lipid pattern that characterizes

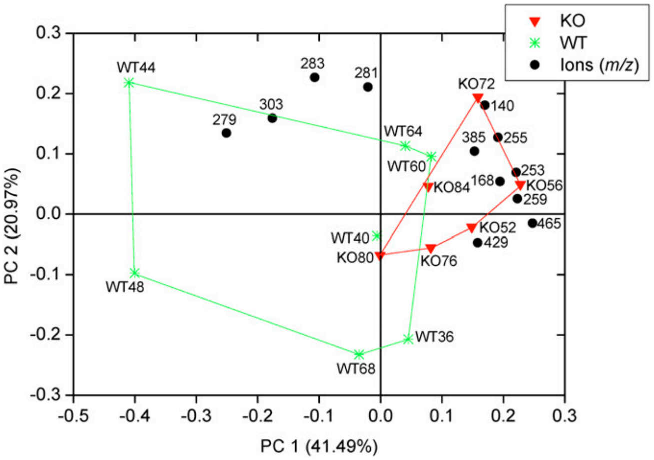

Fig. 6. Biplot on the first two principal components. This graphic permits to simultaneously represent the WT and CF scores and the loadings on the first two principal components. WT mice are represented in green and CF mice in red. CF, cystic fibrosis; KO, knockout; PC1–4, principal component 1–4; WT, wild-type.

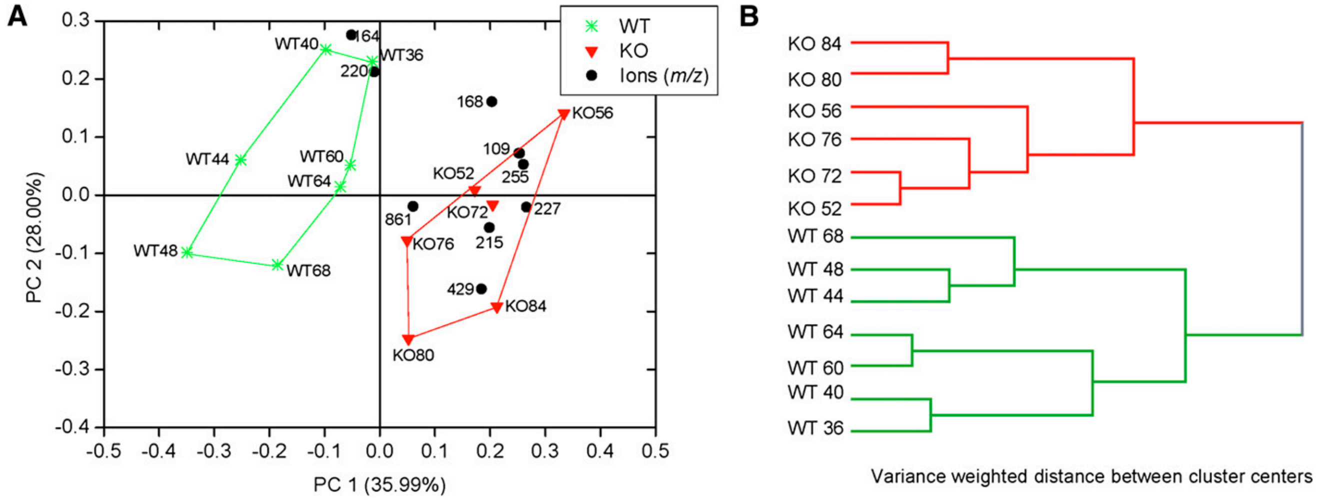

Fig. 7. Separation of WT and CF mice by PCA, and hierarchical clustering of ions selected by GA analysis and listed in Table 2. WT mice are represented in green and CF in red. A: Biplot simultaneously representing WT and CF scores and the loadings on the first two principal components. B: Dendrogram showing the separation of WT and CF mice obtained by hierarchical clustering analysis. This distinction occurs at the first branching, indicating that it is the most characteristic feature among the 13 experiments. CF, cystic fibrosis; GA, genetic algorithm; KO, knockout; PC1–4, principal component 1–4; PCA, principal component analysis; WT, wild-type.

the different histological structures of colonic mucosa, some of them attributable to the differentiation state of intestinal epithelial cells. In addition, slight differences between CF and WT mice in fatty acids, vE, and several phospholipid fragments have been recurrently shown by both univariate and multivariate approaches.

Nevertheless, the results presented in this article cannot be assumed in terms of absolute quantitative data. Note that cluster TOF-SIMS does not allow an absolute quantification. As an imaging technique, only the relative quantification of an individual ion on a surface can be provided. In addition, quantitative comparison between different ions is possible only if they are physicochemically close.

Intestinal mucosa is characterized by intense cell differentiation and turnover. In our study, this fact is suggested by the color variations observed in the different parts of the LG (Fig. 4). Differential lipid content of intestinal epithelial cells related to their differentiation status has been reported (42, 43). Activity of fatty acid desaturases (44) and lipid content is also modified in colonic Caco-2 cells (45) as a function of differentiation. These changes can be associated with the development of the mucosal barrier, as well as the permeability and functional properties of the intestinal mucosa. Nevertheless, our technique eliminates the bias due to cell purification and introduces the analytical accuracy of mass spectrometry. Interestingly, in the case of fatty acid desaturases (44), our results suggest an intense Δ5-desaturase activity in *lamina propria*, border, and submucosa, according to the presence of AA and absence of its precursor C20:3 (supplementary Fig. II).

To our knowledge, the present study constitutes the first attempt to establish a detailed mapping of the lipid content in colonic mucosa. Our results seem to be in agreement with a recent report based on TOF-SIMS imaging of rat duodenum (46). In this seminal study, strong signals corresponding to C16:0 and to the PI polar head (*m/z* 241) were found in the Lieberkühn crypt region; whereas the C18:2 signal was weak in the crypt and strong in the villus, C18:1 was predominant in villi, and C18:0 was ubiquitous (46). In our study, C18:2, an essential fatty acid, was mainly found in the epithelial border (Fig. 1B, J; supplementary Fig. VI). Even though most of the nutrient absorption takes place at the jejunum, the presence of an essential fatty acid, (i.e., exogenous) in this area may denote an intense absorptive activity. In fact, medium chain fatty acids, in particular C18, have been reported to be readily absorbed in the colon (47). The authors suggest that this could compensate for alterations in fatty acid absorption in the small intestine. It has also been demonstrated that the mucin present in the lumen of the digestive tract are able to bind fatty acids and that these could act as a shield against oxygen radicals (48, 49). Note that in our study C20:4 (supplementary Figs. III, IV, V) also presented this type of distribution. This result is consistent with a previous report indicating higher n-6 polyunsaturated fatty acid content in differentiated versus nondifferentiated CaCo-2 cells (45). A more intense biosynthetic activity of differentiated border cells could account in part for this particular distribution.

A remarkable finding in our study is the partial colocalization of C18:2 and CS at the epithelial border (Fig. 1B, E, J, M; supplementary Fig. VII). CS is known to be present in the intestinal epithelium of different animal species (50). It has also been shown, along with other sulfated lipids, to inhibit pancreatic trypsin, chymotrypsin (51), and elastase (50) in a mechanism aimed at protecting the epithelium against the enzyme-rich environment that characterizes the intestinal lumen. However, this is the first time, to our knowledge, that the precise localization of CS at the colon epithelial border is reported.

Particularly surprising was the distribution of the ion at *m/z* 259 (Fig. 1F, N; supplementary Fig. VIII) with localized clusters, not spatially correlated with any other ion or tissue structure. This ion could correspond to the PI polar head (phosphoinositol), or an ST ion, or both. The fact that it colocalizes with the sulfate ion (*m/z* 79.96, not shown) favors the second option. STs are a class of sulfated galactocerebrosides that are characteristic of the peripheral nervous system but are also present in other tissues. However, little is known about their presence and function in the intestine, apart from participating in specialized microdomains involved in the apical trafficking in polarized cultured enterocytes (52). This does not discard the contribution of phosphinositol to the particular distribution of this ion. In fact, phosphatidylinositol kinase plays a pivotal role in the regulation of differentiation, survival, and anoikis of enterocytes, colonocytes, and goblet cells, associated with the Akt1 signaling pathway (53–58). Therefore, it could be expected that a differential content of phosphoinositides was present, depending on the differentiation status of cells. Techniques like the one described in the this article may help to increase the knowledge on the spatial distribution and regulation of differentiation and other important events in intestinal physiology, such as proliferation, apoptosis, anaikis, and electrolyte transport.

The second main objective of the present study was to establish differences in the lipid content and/or in the lipid spatial distribution between WT and CF mice. The differences found were limited to a slight but significant increase in C16:0 and vE in CF colon border. The former can be consistent with an increased saturation of membranes concomitant with a decrease in the presence of polyunsaturated species, while the latter can be attributed to an increased oxidative stress scenario. In fact, the well-documented lipid alterations associated with CF consist, for the most part, of decreased essential and polyunsaturated fatty acid levels in blood (59) and tissues (59, 60) from patients, animal (13, 60), and cell models (61), with a trend toward an imbalance favoring n-6 series biosynthesis (11, 61), as well as decreased choline-containing phospholipids in plasma (12). In our study, no significant differences were detected in either polyunsaturated acid content or distribution. Note that the only reference to date on a fatty acid imbalance in the intestine corresponds to the ileum (60); the reported imbalances corresponded to total tissue homogenates, and in our study, to restricted regions of interest. It is known that other pathologies affecting the colon also present alterations in fatty acid content. Colonic adenocarcinoma has been associated with increased saturated fatty acid ratios (62). The fatty acid content of Crohn's diseased ileal and colonic mucosa has been characterized (63), showing that inflamed mucosa is characterized by a decrease in C18:2 and C18:3 accompanied by a substantial increase in the highly polyunsaturated fatty acids C20:4n-6, C22:4n-6, and C22:6n-3. Ceramide accumulation and lysophosphatidylcholine decrease have been reported as a consequence of experimental colonic inflammation in mouse (64). However, it must be pointed out that inflammation is not the main alteration in the CF knockout mouse model, and similar lipid alterations are not likely to be present.

With respect to vE changes, a deficit in serum vE in CF patients, attributed to intestinal malabsorption, is widely accepted (65, 66). This is believed to contribute to a redox imbalance, and vE supplementation is routinely provided to patients (67). In addition, serum vE content is decreased in pancreatic-insufficient patients at the onset of pulmonary exacerbations (68). These results are consistent with a decrease of vE in liver (69). However, to our knowledge, the content of this vitamin in intestinal mucosa had not been addressed before. The fact that only the ROI delineating the epithelial border shows this difference points to the hypothesis of a potential deficit in absorption.

Whether the observed differences are indicative of an epithelial dysfunction remains to be demonstrated. It is assumed that the small number of samples can be a limiting factor. In any case, the lack of dramatic differences may also be due to the fact that most of absorptive function happens in the small intestine. Subsequently, the consequences of malabsorption should be less remarkable in the colon. Therefore, in this part of the intestine, it would be expected that any differences found in lipid content and/or distribution would be due, for the most part, to defective CFTR-related electrolyte transport. In view of this, it could be argued that lipid abnormalities associated with CF are not directly linked to the regulation of electrolyte transport by CFTR but with other CFTR functions (8).

The main added value of our study is the detailed mapping of lipids obtained by the combined approach of mass spectrometry imaging and multivariate statistical analysis. The analysis of lipids in colonic mucosa has seldom been addressed and employed classic techniques, consisting mostly of a fatty acid profiling (62, 63). PCA and partitioning clustering applied to mass spectrometry imaging data enables us to distinguish the different tissue regions according to their histochemical lipid profiles without resorting to invasive chemicals, such as histological staining (70, 71). In our study, K-mean partitioning into five areas (Fig. 5D) is in good agreement with the histochemical structure shown by optical microscopy (Fig. 1G, O), as well as with the overlay image obtained with PC1, PC2, and PC3 (Fig. 4). In our study, PCA differentiated the main histological areas of the colon section and identified the lipid profiles responsible for this distinction. Our results highlight the very heterogeneous distribution of lipids within the tissue and represents a perfect example of differential lipidome associated with differential function and metabolic state of the cell types present in colon mucosa. This observation can be attributed to the differentiation status of epithelial cells in a tissue were the turnover is especially fast. Our data can provide clues about differentiation mechanisms and a model for other tissues. The differences found between proximal and distal parts of LG present in the four- and five-class clusters (Fig. 5C, D), as well as the color shift in the superposed PC1-PC2-PC3 ion images (Fig. 4), can serve as putative markers of cell differentiation.

It is noteworthy that, in spite of the limited number of samples subjected to our study and the slight differences between WT and CF obtained by semiquantitative univariate analyses, PCA and hierarchical clustering were able to somehow discriminate the two types of mice. This result is in accordance with the fact that the main information in a dataset usually is not carried by a single variable but, rather, by how each variable changes in comparison with other variables (i.e., not how a single lipid is modified but how a subset of lipids covaries). The discriminating set of variables must be considered like a single lipid signature. However, the results reported must be taken cautiously, as some of the variables selected by the genetic algorithm analysis, which allows a better separation (Fig. 7; Table 2), correspond to low abundance fragments of ambiguous origin as their masses are not specific to a particular lipid class. Thus, ion identification as a crucial step in the interpretation of the results provided by this technique.

Nevertheless and despite that the robustness of our study needs to be validated by a series of experiments, it can be concluded that multivariate approaches, such as PCA, are of particular interest to establish differences between models corresponding to two or more pathological states. This study can be considered a proof of concept for further tissue analysis in CF, for pathologies affecting colon, and for tissue-scale functional investigations in the intestinal environment.

REFERENCES

1. Littlewood, J. M. 1992. Cystic fibrosis: gastrointestinal complications. *Br. Med. Bull.* **48:** 847–859.
2. Mascarenhas, M. R. 2003. Treatment of gastrointestinal problems in cystic fibrosis. *Curr. Treat. Options Gastroenterol.* **6:** 427–441.
3. Raia, V., L. Maiuri, G. de Ritis, B. de Vizia, L. Vacca, R. Conte, S. Auricchio, and M. Londei. 2000. Evidence of chronic inflammation in morphologically normal small intestine of cystic fibrosis patients. *Pediatr. Res.* **47:** 344–350.
4. Smyth, R. L., N. M. Croft, U. O'Hea, T. G. Marshall, and A. Ferguson. 2000. Intestinal inflammation in cystic fibrosis. *Arch. Dis. Child.* **82:** 394–399.
5. Brouillard, F., N. Bensalem, A. Hinzpeter, D. Tondelier, S. Trudel, A. D. Gruber, M. Ollero, and A. Edelman. 2005. Blue native/SDS-PAGE analysis reveals reduced expression of the mClCA3 protein in cystic fibrosis knock-out mice. *Mol. Cell. Proteomics.* **4:** 1762–1775.
6. Eckman, E. A., C. U. Cotton, D. M. Kube, and P. B. Davis. 1995. Dietary changes improve survival of CFTR S489X homozygous mutant mouse. *Am. J. Physiol.* **269:** L625–L630.
7. Norkina, O., S. Kaur, D. Ziemer, and R. C. De Lisle. 2004. Inflammation of the cystic fibrosis mouse small intestine. *Am. J. Physiol. Gastrointest. Liver Physiol.* **286:** G1032–G1041.
8. Ollero, M., F. Brouillard, and A. Edelman. 2006. Cystic fibrosis enters the proteomics scene: new answers to old questions. *Proteomics.* **6:** 4084–4099.
9. Worgall, T. S. 2009. Lipid metabolism in cystic fibrosis. *Curr. Opin. Clin. Nutr. Metab. Care.* **12:** 105–109.
10. Freedman, S. D., P. G. Blanco, M. M. Zaman, J. C. Shea, M. Ollero, I. K. Hopper, D. A. Weed, A. Gelrud, M. M. Regan, M. Laposata, et al. 2004. Association of cystic fibrosis with abnormalities in fatty acid metabolism. *N. Engl. J. Med.* **350:** 560–569.
11. Ollero, M., M. Laposata, M. M. Zaman, P. G. Blanco, C. Andersson, J. Zeind, Y. Urman, G. Kent, J. G. Alvarez, and S. D. Freedman. 2006. Evidence of increased flux to n-6 docosapentaenoic acid in phospholipids of pancreas from cftr$^{-/-}$ knockout mice. *Metabolism.* **55:** 1192–1200.
12. Guerrera, I. C., G. Astarita, J. P. Jais, D. Sands, A. Nowakowska, J. Colas, I. Sermet-Gaudelus, M. Schuerenberg, D. Piomelli, A. Edelman, et al. 2009. A novel lipidomic strategy reveals plasma phospholipid signatures associated with respiratory disease severity in cystic fibrosis patients. *PLoS ONE.* **4:** e7735.
13. Dombrowsky, H., G. T. Clark, G. A. Rau, W. Bernhard, and A. D. Postle. 2003. Molecular species compositions of lung and pancreas phospholipids in the cftr(tm1HGU/tm1HGU) cystic fibrosis mouse. *Pediatr. Res.* **53:** 447–454.
14. Guilbault, C., G. Wojewodka, Z. Saeed, M. Hajduch, E. Matouk, J. B. De Sanctis, and D. Radzioch. 2009. Cystic fibrosis fatty acid imbalance is linked to ceramide deficiency and corrected by fenretinide. *Am. J. Respir. Cell Mol. Biol.* **41:** 100–106.
15. Teichgraber, V., M. Ulrich, N. Endlich, J. Riethmuller, B. Wilker, C. C. De Oliveira-Munding, A. M. van Heeckeren, M. L. Barr, G. von Kurthy, K. W. Schmid, et al. 2008. Ceramide accumulation mediates inflammation, cell death and infection susceptibility in cystic fibrosis. *Nat. Med.* **14:** 382–391.
16. White, N. M., D. Jiang, J. D. Burgess, I. R. Bederman, S. F. Previs, and T. J. Kelley. 2007. Altered cholesterol homeostasis in cultured and in vivo models of cystic fibrosis. *Am. J. Physiol. Lung Cell. Mol. Physiol.* **292:** L476–L486.
17. Benninghoven, A., and E. Loebach. 1971. Tandem mass spectrometer for secondary ion studies. *Rev. Sci. Instrum.* **42:** 49–52.
18. Castaing, R., and G. J. Slodzian. 1962. Microanalyse par émission ionique secondaire. *J. Microsc. (Paris).* **1:** 395–410.
19. Benabdellah, F., A. Seyer, L. Quinton, D. Touboul, A. Brunelle, and O. Laprévote. 2010. Mass spectrometry imaging of rat brain sections: nanomolar sensitivity with MALDI versus nanometer resolution by TOF-SIMS. *Anal. Bioanal. Chem.* **396:** 151–162.
20. Biddulph, G. X., A. M. Piwowar, J. S. Fletcher, N. P. Lockyer, and J. C. Vickerman. 2007. Properties of C84 and C24H12 molecular ion sources for routine TOF-SIMS analysis. *Anal. Chem.* **79:** 7259–7266.
21. Sjövall, P., J. Lausmaa, and B. Johansson. 2004. Mass spectrometric imaging of lipids in brain tissue. *Anal. Chem.* **76:** 4271–4278.
22. Touboul, D., F. Halgand, A. Brunelle, R. Kersting, E. Tallarek, B. Hagenhoff, and O. Laprévote. 2004. Tissue molecular ion imaging by gold cluster ion bombardment. *Anal. Chem.* **76:** 1550–1559.
23. Touboul, D., F. Kollmer, E. Niehuis, A. Brunelle, and O. Laprévote. 2005. Improvement of biological time-of-flight-secondary ion mass spectrometry imaging with a bismuth cluster ion source. *J. Am. Soc. Mass Spectrom.* **16:** 1608–1618.
24. Weibel, D., S. Wong, N. Lockyer, P. Blenkinsopp, R. Hill, and J. C. Vickerman. 2003. A C60 primary ion beam system for time of flight secondary ion mass spectrometry: its development and secondary ion yield characteristics. *Anal. Chem.* **75:** 1754–1764.
25. Brunelle, A., and O. Laprévote. 2009. Lipid imaging with cluster time-of-flight secondary ion mass spectrometry. *Anal. Bioanal. Chem.* **393:** 31–35.
26. Brunelle, A., and O. Laprévote. 2007. Recent advances in biological tissue imaging with time-of-flight secondary ion mass spectrometry: polyatomic ion sources, sample preparation, and applications. *Curr. Pharm. Des.* **13:** 3335–3343.
27. Brunelle, A., D. Touboul, and O. Laprévote. 2005. Biological tissue imaging with time-of-flight secondary ion mass spectrometry and cluster ion sources. *J. Mass Spectrom.* **40:** 985–999.
28. Debois, D., M. P. Bralet, F. Le Naour, A. Brunelle, and O. Laprévote. 2009. In situ lipidomic analysis of nonalcoholic fatty liver by cluster TOF-SIMS imaging. *Anal. Chem.* **81:** 2823–2831.
29. Le Naour, F., M. P. Bralet, D. Debois, C. Sandt, C. Guettier, P. Dumas, A. Brunelle, and O. Laprévote. 2009. Chemical imaging on liver steatosis using synchrotron infrared and ToF-SIMS microspectroscopies. *PLoS ONE.* **4:** e7408.
30. Mas, S., D. Touboul, A. Brunelle, P. Aragoncillo, J. Egido, O. Laprévote, and F. Vivanco. 2007. Lipid cartography of atherosclerotic plaque by cluster-TOF-SIMS imaging. *Analyst (Lond.).* **132:** 24–26.
31. Tahallah, N., A. Brunelle, S. De La Porte, and O. Laprévote. 2008. Lipid mapping in human dystrophic muscle by cluster-time-of-flight secondary ion mass spectrometry imaging. *J. Lipid Res.* **49:** 438–454.
32. Touboul, D., A. Brunelle, F. Halgand, S. De La Porte, and O. Laprévote. 2005. Lipid imaging by gold cluster time-of-flight secondary ion mass spectrometry: application to Duchenne muscular dystrophy. *J. Lipid Res.* **46:** 1388–1395.
33. Trim, P. J., S. J. Atkinson, A. P. Princivalle, P. S. Marshall, A. West, and M. R. Clench. 2008. Matrix-assisted laser desorption/ionisation mass spectrometry imaging of lipids in rat brain tissue with integrated unsupervised and supervised multivariant statistical analysis. *Rapid Commun. Mass Spectrom.* **22:** 1503–1509.
34. Piras, F. M., M. F. Dettori, and A. Magnani. 2009. ToF-SIMS PCA analysis of *Myrtus communis* L. *Appl. Surf. Sci.* **255:** 7805–7811.

35. Magnusson, Y. K., P. Friberg, P. Malmberg, and Y. Chen. 2008. Application of multivariate analysis of TOF-SIMS spectra for studying the effect of high glucose intake on aortic lipid profile. *Appl. Surf. Sci.* **254:** 6580–6585.
36. Borner, K., H. Nygren, B. Hagenhoff, P. Malmberg, E. Tallarek, and J. E. Mansson. 2006. Distribution of cholesterol and galactosylceramide in rat cerebellar white matter. *Biochim. Biophys. Acta.* **1761:** 335–344.
37. Heim, C., P. Sjövall, J. Lausmaa, T. Leefmann, and V. Thiel. 2009. Spectral characterisation of eight glycerolipids and their detection in natural samples using time-of-flight secondary ion mass spectrometry. *Rapid Commun. Mass Spectrom.* **23:** 2741–2753.
38. Magnusson, Y. K., P. Friberg, P. Sjövall, J. Malm, and Y. Chen. 2008. TOF-SIMS analysis of lipid accumulation in the skeletal muscle of ob/ob mice. *Obesity (Silver Spring).* **16:** 2745–2753.
39. Monroe, E. B., J. C. Jurchen, J. Lee, S. S. Rubakhin, and J. V. Sweedler. 2005. Vitamin E imaging and localization in the neuronal membrane. *J. Am. Chem. Soc.* **127:** 12152–12153.
40. Vickerman, J. C. 2001. ToF-SIMS: an overview. *In* ToF-SIMS: Surface Analysis by Mass Spectrometry. J. C. Vickerman and D. Briggs, eds. SurfaceSpectra and IM Publications, Manchester. 1–40.
41. Gilmore, I. S., and M. P. Seah. 2002. Electron flood gun damage in the analysis of polymers and organics in time-of-flight SIMS. *Appl. Surf. Sci.* **187:** 89–100.
42. Alessandri, J. M., T. S. Arfi, J. Thevenoux, and C. L. Leger. 1990. Diet-induced alterations of lipids during cell differentiation in the small intestine of growing rats: effect of an essential fatty acid deficiency. *J. Pediatr. Gastroenterol. Nutr.* **10:** 504–515.
43. Brasitus, T. A., and P. K. Dudeja. 1985. Alterations in the physical state and composition of brush border membrane lipids of rat enterocytes during differentiation. *Arch. Biochem. Biophys.* **240:** 483–488.
44. Dias, V. C., and H. G. Parsons. 1995. Modulation in delta 9, delta 6, and delta 5 fatty acid desaturase activity in the human intestinal CaCo-2 cell line. *J. Lipid Res.* **36:** 552–563.
45. Jindrichova, S., O. Novakova, J. Bryndova, E. Tvrzicka, V. Lisa, F. Novak, and J. Pacha. 2003. Corticosteroid effect on Caco-2 cell lipids depends on cell differentiation. *J. Steroid Biochem. Mol. Biol.* **87:** 157–165.
46. Richter, K., H. Nygren, P. Malmberg, and B. Hagenhoff. 2007. Localization of fatty acids with selective chain length by imaging time-of-flight secondary ion mass spectrometry. *Microsc. Res. Tech.* **70:** 640–647.
47. Jorgensen, J. R., M. D. Fitch, P. B. Mortensen, and S. E. Fleming. 2002. Absorption and metabolism of octanoate by the rat colon in vivo: concentration dependency and influence of alternative fuels. *Gut.* **51:** 76–81.
48. Gong, D. H., B. Turner, K. R. Bhaskar, and J. T. Lamont. 1990. Lipid binding to gastric mucin: protective effect against oxygen radicals. *Am. J. Physiol.* **259:** G681–G686.
49. Krause, W. J. 2000. Brunner's glands: a structural, histochemical and pathological profile. *Prog. Histochem. Cytochem.* **35:** 259–267.
50. Ito, N., Y. Iwamori, K. Hanaoka, and M. Iwamori. 1998. Inhibition of pancreatic elastase by sulfated lipids in the intestinal mucosa. *J. Biochem.* **123:** 107–114.
51. Iwamori, M., Y. Iwamori, and N. Ito. 1997. Sulfated lipids as inhibitors of pancreatic trypsin and chymotrypsin in epithelium of the mammalian digestive tract. *Biochem. Biophys. Res. Commun.* **237:** 262–265.
52. Delacour, D., V. Gouyer, J. P. Zanetta, H. Drobecq, E. Leteurtre, G. Grard, O. Moreau-Hannedouche, E. Maes, A. Pons, S. Andre, et al. 2005. Galectin-4 and sulfatides in apical membrane trafficking in enterocyte-like cells. *J. Cell Biol.* **169:** 491–501.
53. Bouchard, V., M. J. Demers, S. Thibodeau, V. Laquerre, N. Fujita, T. Tsuruo, J. F. Beaulieu, R. Gauthier, A. Vezina, L. Villeneuve, et al. 2007. Fak/Src signaling in human intestinal epithelial cell survival and anoikis: differentiation state-specific uncoupling with the PI3-K/Akt-1 and MEK/Erk pathways. *J. Cell. Physiol.* **212:** 717–728.
54. Dufour, G., M. J. Demers, D. Gagne, A. B. Dydensborg, I. C. Teller, V. Bouchard, I. Degongre, J. F. Beaulieu, J. Q. Cheng, N. Fujita, et al. 2004. Human intestinal epithelial cell survival and anoikis. Differentiation state-distinct regulation and roles of protein kinase B/Akt isoforms. *J. Biol. Chem.* **279:** 44113–44122.
55. Durual, S., C. Blanchard, M. Estienne, M. F. Jacquier, J. C. Cuber, V. Perrot, C. Laboisse, and J. C. Cuber. 2005. Expression of human TFF3 in relation to growth of HT-29 cell subpopulations: involvement of PI3-K but not STAT6. *Differentiation.* **73:** 36–44.
56. Laprise, P., P. Chailler, M. Houde, J. F. Beaulieu, M. J. Boucher, and N. Rivard. 2002. Phosphatidylinositol 3-kinase controls human intestinal epithelial cell differentiation by promoting adherens junction assembly and p38 MAPK activation. *J. Biol. Chem.* **277:** 8226–8234.
57. Li, X., S. Leu, A. Cheong, H. Zhang, B. Baibakov, C. Shih, M. J. Birnbaum, and M. Donowitz. 2004. Akt2, phosphatidylinositol 3-kinase, and PTEN are in lipid rafts of intestinal cells: role in absorption and differentiation. *Gastroenterology.* **126:** 122–135.
58. Vachon, P. H., C. Harnois, A. Grenier, G. Dufour, V. Bouchard, J. Han, J. Landry, J. F. Beaulieu, A. Vezina, A. B. Dydensborg, et al. 2002. Differentiation state-selective roles of p38 isoforms in human intestinal epithelial cell anoikis. *Gastroenterology.* **123:** 1980–1991.
59. Farrell, P. M., E. H. Mischler, M. J. Engle, D. J. Brown, and S. M. Lau. 1985. Fatty acid abnormalities in cystic fibrosis. *Pediatr. Res.* **19:** 104–109.
60. Freedman, S. D., M. H. Katz, E. M. Parker, M. Laposata, M. Y. Urman, and J. G. Alvarez. 1999. A membrane lipid imbalance plays a role in the phenotypic expression of cystic fibrosis in cftr(−/−) mice. *Proc. Natl. Acad. Sci. USA.* **96:** 13995–14000.
61. Andersson, C., M. R. Al-Turkmani, J. E. Savaille, R. Alturkmani, W. Katrangi, J. E. Cluette-Brown, M. M. Zaman, M. Laposata, and S. D. Freedman. 2008. Cell culture models demonstrate that CFTR dysfunction leads to defective fatty acid composition and metabolism. *J. Lipid Res.* **49:** 1692–1700.
62. Rakheja, D., P. Kapur, M. P. Hoang, L. C. Roy, and M. J. Bennett. 2005. Increased ratio of saturated to unsaturated C18 fatty acids in colonic adenocarcinoma: implications for cryotherapy and lipid raft function. *Med. Hypotheses.* **65:** 1120–1123.
63. Buhner, S., E. Nagel, J. Korber, H. Vogelsang, T. Linn, and R. Pichlmayr. 1994. Ileal and colonic fatty acid profiles in patients with active Crohn's disease. *Gut.* **35:** 1424–1428.
64. Bauer, J., G. Liebisch, C. Hofmann, C. Huy, G. Schmitz, F. Obermeier, and J. Bock. 2009. Lipid alterations in experimental murine colitis: role of ceramide and imipramine for matrix metalloproteinase-1 expression. *PLoS ONE.* **4:** e7197.
65. Homnick, D. N., J. H. Cox, M. J. DeLoof, and T. V. Ringer. 1993. Carotenoid levels in normal children and in children with cystic fibrosis. *J. Pediatr.* **122:** 703–707.
66. Lancellotti, L., C. D'Orazio, G. Mastella, G. Mazzi, and U. Lippi. 1996. Deficiency of vitamins E and A in cystic fibrosis is independent of pancreatic function and current enzyme and vitamin supplementation. *Eur. J. Pediatr.* **155:** 281–285.
67. Huang, S. H., J. I. Schall, B. S. Zemel, and V. A. Stallings. 2006. Vitamin E status in children with cystic fibrosis and pancreatic insufficiency. *J. Pediatr.* **148:** 556–559.
68. Hakim, F., E. Kerem, J. Rivlin, L. Bentur, H. Stankiewicz, T. Bdolach-Abram, and M. Wilschanski. 2007. Vitamins A and E and pulmonary exacerbations in patients with cystic fibrosis. *J. Pediatr. Gastroenterol. Nutr.* **45:** 347–353.
69. Underwood, B. A., and C. R. Denning. 1972. Blood and liver concentrations of vitamins A and E in children with cystic fibrosis of the pancreas. *Pediatr. Res.* **6:** 26–31.
70. McCombie, G., D. Staab, M. Stoeckli, and R. Knochenmuss. 2005. Spatial and spectral correlations in MALDI mass spectrometry images by clustering and multivariate analysis. *Anal. Chem.* **77:** 6118–6124.
71. Eijkel, G. B., B. K. Kaletas, I. M. van der Wiel, J. M. Kros, T. M. Luider, and R. M. A. Heeren. 2009. Correlating MALDI and SIMS imaging mass spectrometric datasets of biological tissue surfaces. *Surf. Interface Anal.* **41:** 675–685.